

Two-step nucleation mechanism in solid–solid phase transitions

Yi Peng,¹ Feng Wang,¹ Zhen Wang,¹ Ahmed M. Alsayed,² Zixin Zhang,³ Arjun S. Ghosh,⁴ and Yilong Han^{1,5*}

The microscopic kinetics of ubiquitous solid–solid phase transitions remain poorly understood. Here, by using single-particle-resolution video microscopy of colloidal filaments, we show that transitions between square and triangular lattices occur via a two-step diffusive nucleation pathway involving liquid nuclei. The nucleation pathway is favoured over the direct one-step nucleation because the energy of the solid/liquid interface is lower than that between solid phases. We also observed that nucleation precursors are particle-swapping loops rather than newly generated structural defects, and that coherent and incoherent facets of the evolving nuclei exhibit different energies and growth rates that can markedly alter the nucleation kinetics. Our findings suggest that an intermediate liquid should exist in the nucleation processes of solid–solid transitions of most metals and alloys, and provide guidance for better control of the kinetics of the transition and for future refinements of solid–solid transition theory.

Solid–solid (s–s) transitions between different crystalline structures are arguably the most numerous of natural phase transitions. Among them are common transformations exhibited by elemental crystals, alloys and minerals¹, with broad implications in earth science², diamond and steel production^{3,4}, and the synthesis of ceramic materials⁴. However, despite their considerable technological importance, the microscopic kinetics of s–s transitions remain poorly understood. The mechanisms that govern s–s phase transitions present substantial challenges for theory, simulation and experiment. A central question about the nature of s–s transitions, for example, concerns their kinetic pathways; in particular, do these pathways follow a diffusionless martensitic transformation with particles moving in concert¹ or a diffusive nucleation process? So far, s–s transitions in atomic and molecular crystals have mainly been studied by means of X-ray diffraction⁵ and electron microscopy^{6–8}—techniques which rarely reveal the initial stage of the s–s transition and the dynamics at the single-particle level. Nevertheless, in experimental studies of graphite–diamond⁹ and olive–spinel systems⁷, diffusive nucleation has been inferred to occur when anisotropic stresses are negligible. Martensitic transformations have been observed in simulations that use small systems¹⁰, strong superheating¹¹ or external anisotropic stresses¹². These three conditions are typically employed to speed up sluggish dynamics in simulations, and tend to promote martensitic transformations and suppress the nucleation mechanism⁶. Consequently, kinetic paths under isotropic stresses remain controversial⁶. Finally, analytical theories are difficult to formulate and are not definitive because of missing group–subgroup relations between the symmetries of parent and product crystals¹³.

Stimulated by these open questions and technical difficulties, our experiments sought to observe nucleation processes in the s–s transitions of colloidal crystals with single-particle resolution. This class of model thermodynamic system, composed of micrometre-sized colloidal particles whose thermal motions can be directly visualized by video microscopy, has already provided many general

insights about phase transitions¹⁴, including the dynamics of crystallization^{15,16}, melting^{17,18}, glass formation²⁰ and jamming transitions²¹. Few such studies, however, have probed s–s transitions, and those that did focused on structure rather than kinetics^{22–25}, and the surfaces or grain boundaries of small-sized crystals^{23,25} and/or external anisotropic fields²² suppressed nucleation. In our experiment, the high-quality large crystalline domains and the local heating technique enable us to study nearly homogeneous nucleation and heterogeneous nucleation at a desired type of defect. We discover a surprising two-step nucleation behaviour during the transformation between square (□) and triangular (Δ) lattices, with an intermediate liquid stage that might be expected to occur in crystals with constituents at any length scale, provided that solid–liquid interfacial energies are sufficiently small. Furthermore, the single-particle experimental resolution enabled us to directly identify liquid nucleation precursors, which arise from particle-swapping loops rather than from defects, and to study the facets of evolving nuclei, whose energetics and growth rates exhibit rich phenomenology.

Experiment

Temperature-sensitive poly(*N*-isopropylacrylamide) (NIPA) microgel colloidal spheres¹⁷ were employed to make the volume-fraction-tunable systems needed for these studies. The NIPA sphere effective diameter, σ , changes linearly from 0.76 μm at 26.4 °C to 0.67 μm at 30.6 °C in water (Supplementary Fig. 1A) and short-range repulsive interactions (Supplementary Fig. 1A) and exhibit almost the same phase behaviour as hard spheres^{17,18}. The refractive index of the NIPA spheres is very close to that of water because water makes up more than 90% of the microgel. Consequently, reasonably clear images of the bulk crystalline layers can be obtained even using bright-field microscopy¹⁷. They form face-centred cubic (fcc) crystals in three dimensions (3D) and triangular lattices in two dimensions (2D). To obtain the multiple crystalline phases needed to probe the s–s transition, the colloidal spheres were

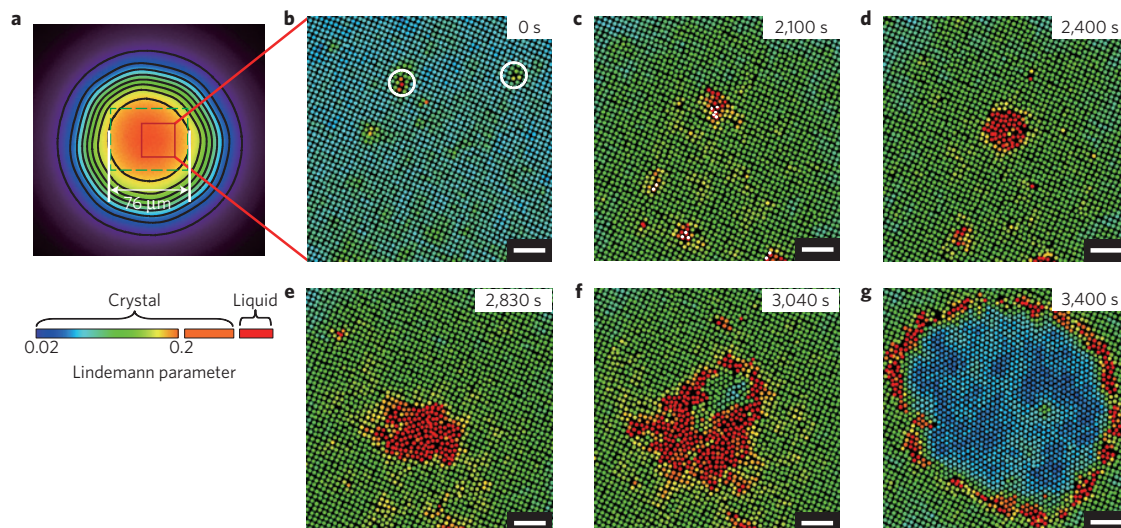


Figure 1 $n\Delta \rightarrow (n-1)\Delta$ two-step nucleation in a crystal with two vacancies in an $H = 3 \mu\text{m}$ sample at 27.2°C . **a**, Steady temperature profile in the xy -plane. The contour spacing is 0.2°C . The temperature difference in the $\pi(38 \mu\text{m})^2$ area of the central circle is less than 0.2°C . The green dashed rectangle is the full field of view. The red square is the area shown in **b–g**. **b–g**, Spatiotemporal evolution of the central region of the crystal during the s – s transition. The colours represent different values of the Lindemann parameter for each particle measured during a 4 s time period (Supplementary Fig. 3). Liquid-like particles in red are defined as particles with low bond-orientational orders and large Lindemann parameters >0.2 (Supplementary Information). Scale bars, $5 \mu\text{m}$. See also Supplementary Movie 2. **b**, At $t = 0$ s, the heating light was switched on. The temperature increased and stabilized in 3 s. Two vacancies are labelled by circles. **c**, At $t = 2,100$ s, particles labelled with white dots are swapping positions with their neighbours, although the overall lattice structure remains intact. **d**, At $t = 2,400$ s, a liquid nucleus has begun to form near one of the vacancies—that is, a vacancy surrounded by particles that are swapping positions—even though the sample state (and temperature) is below the melting point. **e**, By $t = 2,830$ s, the liquid nucleus has grown larger. **f**, At $t = 3,040$ s, a Δ -lattice nucleus has developed within a liquid nucleus that exceeds the critical size. **g**, By $t = 3,400$ s, the Δ -lattice nucleus has grown larger, well beyond its critical size.

confined between two glass walls. Such samples are well known to exhibit a cascade of crystalline phases as a function of increasing wall separation H : $1\Delta, 2\Delta, 2\Delta, 3\Delta, 3\Delta, \dots$ (refs 26–28). Here 1Δ denotes a monolayer triangular lattice; 2Δ denotes a two-layer square lattice, and so on. Similar structures have been found in plasmas²⁹ and in electron bilayers of semiconductors³⁰. The equilibrium state of these samples is controlled by two thermodynamic variables: the ratio of wall separation to particle diameter, H/σ , and the particle volume fraction ϕ (refs 27,28). When temperature is varied, σ changes and thus both H/σ and ϕ are varied concurrently to produce $n\Delta \rightarrow (n-1)\Delta$ transitions. If temperature is varied quasi-statically, then such systems evolve along an angled trajectory in the phase diagram (Supplementary Fig. 2B). Here, we varied temperature suddenly to produce a superheated metastable $n\Delta$ -lattice, and then monitored its evolution towards the equilibrium $(n-1)\Delta$ -lattice at a constant temperature (that is, at constant H/σ and ϕ).

When the whole sample was heated, $n\Delta \rightarrow (n-1)\Delta$ transitions always occurred without nucleation; transitions began at the interfaces between $n\Delta$ and $(n-1)\Delta$ domains (Supplementary Movie 1). Therefore, to prevent invasion from pre-existing $(n-1)\Delta$ domains, we devised a scheme whereby a beam of light passing through the microscope objective lens locally heated the interior of an $n\Delta$ crystalline domain with a typical size of 10^5 particles per layer¹⁸. The heated area equilibrated to a temperature of $T_{\text{amb}} + \delta T$. The ambient temperature, T_{amb} , was adjustable with 0.1°C resolution using temperature controllers on the microscope, and the optical heating typically induced a local temperature change of $\delta T = 1.6^\circ\text{C}$ near the centre of the illumination region (Fig. 1a). The temperature attained its steady-state value ~ 3 s after the light was turned on (Supplementary Fig. 1C; ref. 18). The s – s transition is achieved when $T_{\text{amb}} < T_{s-s} < T_{\text{amb}} + \delta T < T_m$, where T_{s-s} and T_m correspond to the s – s and melting (solid–liquid) transitions, respectively.

In our experiments, the incubation time before a nucleus forms ranges from 5 to 60 min, depending on the degree of superheating.

This incubation time is thus much larger than the temperature equilibration time of 3 s. The temperature was set to be constant for the entire duration of the incubation and nucleation processes, and was measured to be very uniform in the central $\pi(38 \mu\text{m})^2$ area of the xy -plane (Fig. 1a) and throughout the thickness (z direction) of the thin films. This $76\text{-}\mu\text{m}$ -diameter region of interest is very small compared to the $18 \times 18 \text{ mm}^2$ sample cell size, and the wall separation is very uniform ($<0.03\sigma$) in the region of interest. Most of the nuclei studied were larger than H and had a uniform shape in the z direction; thus we monitored only a fixed layer within the thin film. In most experiments we monitored the surface layer, wherein liquid-like particles are more clearly distinguished and characterized. The particle motions were recorded with a charge-coupled device (CCD) camera at 10 frames s^{-1} . Particle positions were tracked using standard image analysis³¹. Experimental details are given in the Methods and Supplementary Information.

Two-step nucleation

Nucleation near vacancies (Fig. 1 and Supplementary Movie 2), dislocations (Fig. 2 and Supplementary Movie 3) and a grain boundary (Fig. 3 and Supplementary Movie 4) was measured by choosing heating areas containing these particular defects. All the superheated metastable crystals exhibited an interesting two-step nucleation pathway: $n\Delta$ -lattice crystal \rightarrow post-critical liquid nucleus \rightarrow $(n-1)\Delta$ -lattice nucleus (Figs 1–3). This behaviour was robust across 50 independent experiments observed inside $n\Delta$ -lattice crystal domains and 6 independent experiments observed at grain boundaries. The largest observed liquid area had ~ 740 particles per layer (Supplementary Movie 5). Liquid-like particles swapped positions in movies, indicating that they are indeed liquid. Note that the intermediate liquid nucleus is in a metastable supercooled state which is denser than the equilibrium liquid phase. In fact, the metastable liquid, the superheated $n\Delta$ -lattice and the final equilibrium $(n-1)\Delta$ -lattice have approximately the same number density

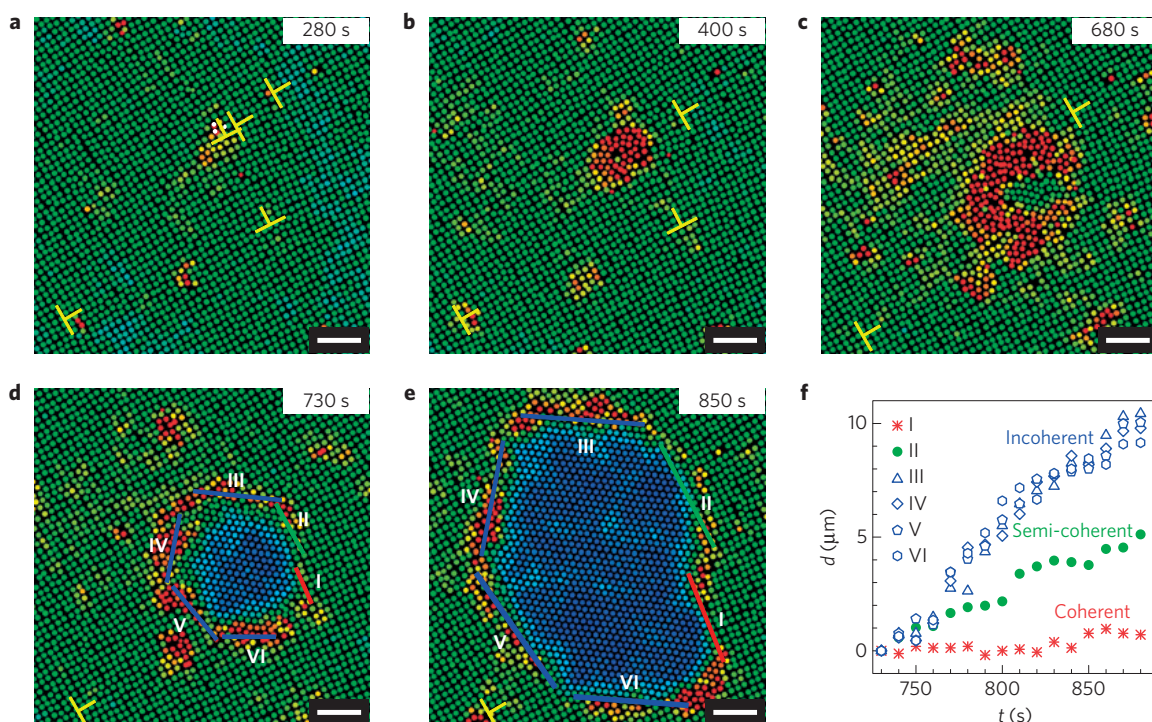


Figure 2 | $5\square \rightarrow 4\Delta$ two-step nucleation in a crystal with dislocations at 27.4°C . Colours represent different values of the Lindemann parameter, as in Fig. 1. Dislocations are labelled by the symbol \perp . Scale bars, $5\ \mu\text{m}$. See also Supplementary Movie 3. **a**, 280 s after switching on the heating light, particles labelled with white dots are swapping positions with their neighbours. **b**, At $t = 400$ s, a liquid nucleus formed in a region wherein coalescence of dislocations and particle-swapping regions occurred. **c**, A Δ -lattice nucleus formed within the post-critical liquid nucleus at $t = 680$ s. **d**, All liquid has transformed to a Δ -lattice at $t = 730$ s. **e**, At $t = 850$ s, the Δ -lattice nucleus has clearly developed facets, which are described as I, coherent; II, semi-coherent; III–VI, coherent. **f**, The displacements of the facets in **e** along the direction normal to the facets.

and volume fraction, because the ambient \square -lattice did not exhibit any measurable distortion. Figure 1 shows liquid nuclei that have developed from within the \square -lattice, including one near a vacancy that grew larger than its critical size (that is, that grew to its post-critical size). Then, at a later time, we see a Δ -lattice nuclei develop within this liquid region (Fig. 1f). Finally, when the Δ -lattice nuclei grows to its post-critical size, the entire liquid region is rapidly transformed into a single Δ -lattice nucleus (Fig. 1g). At this point, the Δ -lattice nucleus grows irreversibly in the sample, indicating that it is much larger than its critical size in the \square -lattice. Importantly, both the liquid nucleus and the Δ -lattice nucleus were observed to grow within their parent phases by monomer diffusion and attachment rather than via concerted motions characteristic of martensitic transformations. The two-step nucleation mechanism was found in all 56 independent colloidal crystal experiments without anisotropic pressures and, although we have focused our discussion on the $5\square \rightarrow 4\Delta$ transitions, the same behaviours were observed in other $n\square \rightarrow (n-1)\Delta$ transitions for $n \neq 5$.

The free energy of a product-phase nucleus within the parent phase is¹ (Supplementary Information):

$$\Delta G = -V\rho\Delta\mu + A\gamma + E_{\text{strain}} - E_{\text{defect}} \quad (1)$$

where A is the nucleus surface area, γ is the surface tension, V is the nucleus volume, ρ is the number density of particles in the nucleus, $\Delta\mu$ (>0) is the chemical potential difference between the parent phase and the nucleus, E_{strain} is the misfit strain energy in the crystal caused by volume changes of the nucleus, and E_{defect} (>0) represents the energy of pre-existing defects in volume V . E_{strain} is zero when the parent phase is a fluid and finite when the parent phase is a solid. The competing terms with opposite signs in equation (1) give rise to a barrier in ΔG as a function of nucleus size. Thus, small nuclei tend

to shrink rather than grow, unless their size exceeds a critical value related to the barrier height of ΔG (Fig. 4a).

The mechanism of the two-step nucleation is shown in Fig. 4. The schematic in Fig. 4a compares the ΔG barriers for the liquid and Δ -lattice nuclei in a \square -lattice (see Supplementary Fig. 5 for a more detailed discussion) as a function of the radius of the nuclei, r . $\Delta G_{\text{liquid}} < \Delta G_{\Delta}$ at small r , whereas $\Delta G_{\text{liquid}} > \Delta G_{\Delta}$ at large r . Hence a small nucleus is first liquid and then transforms into a Δ -lattice nucleus when it becomes large—that is, the system follows the path with the lowest ΔG in Fig. 4a.

The two-step nucleation can be understood with the aid of Fig. 4b, which shows coexisting triangular and liquid nuclei in the square parent phase. The contact angles of the Δ -lattice at all \square - Δ -liquid junctions are less than 90° , which suggests that $\gamma_{\square-\Delta} < \gamma_{\square-\text{liquid}}$ —that is, because force balance at the interface of the \square -crystal requires $\gamma_{\square-\Delta} + \cos\alpha \cdot \gamma_{\Delta-\text{liquid}} = \gamma_{\square-\text{liquid}}$. A liquid nucleus is more favourable in the \square -crystal parent phase than a Δ -lattice nuclei in the \square -crystal because the surface-energy term $A\gamma$ in equation (1) dominates for small nuclei. However, when the liquid nucleus is large, the bulk terms of chemical potential and strain energy in equation (1) dominate, and the nucleus will transform into a Δ -lattice (see Supplementary Information for a more detailed discussion). This mechanism clearly works in 2D, 3D and even thin-film crystals, as the film-wall interfacial energy can be absorbed into the bulk term in equation (1) without any contribution to the surface term (Supplementary Information). The same analysis can be applied near defects, because defects lower both barriers in Fig. 4a by the same amount, E_{defect} , in equation (1). Thus defects do not drive the two-step nucleation, and crystals with and without defects should exhibit similar two-step behaviours (Figs 1–3).

The two-step nucleation provides a real-space illustration of the Ostwald's step rule, sketched in Fig. 4c: instead of transforming

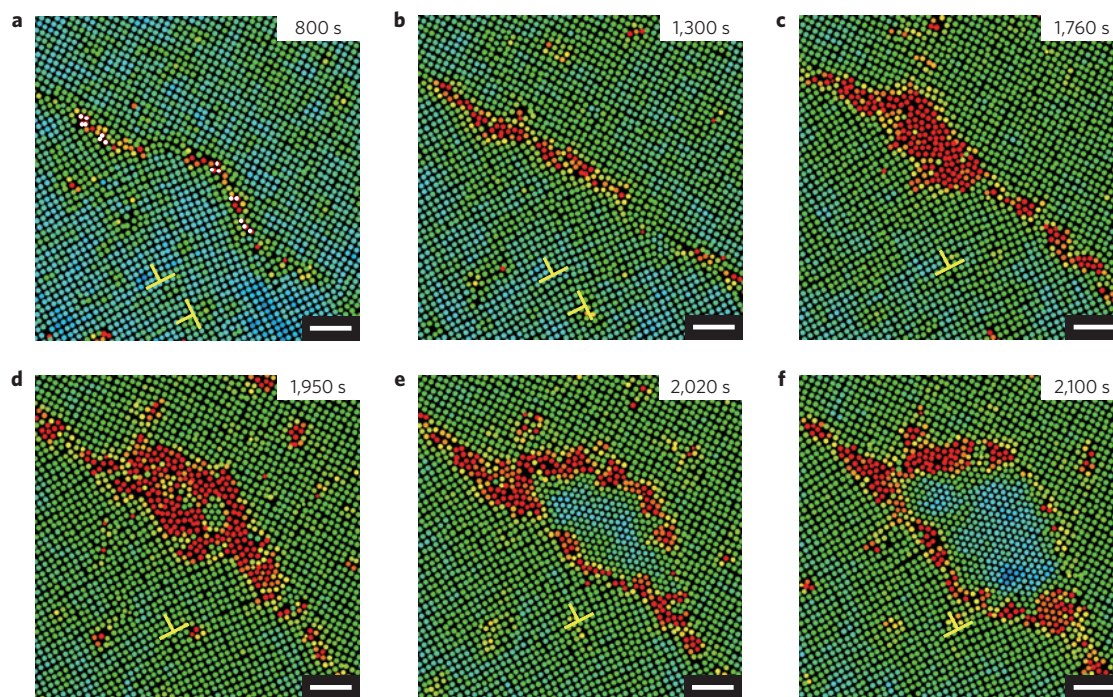


Figure 5 $\square \rightarrow \Delta$ two-step nucleation at a grain boundary at 27.2°C . Colours represent different values of the Lindemann parameter, as in Fig. 1. Scale bars, $5\ \mu\text{m}$. See also Supplementary Movie 4. **a**, Particle swapping (white dots) occurred only at the grain boundary. **b**, The liquid first coalesced into a large elongated nucleus. **c**, The liquid then grew into an asymmetric droplet relative to the grain boundary because the grain boundary has different angles relative to the two \square -lattices. **d**, The Δ -lattice nucleated from within a liquid nucleus. **e, f**, The nucleated Δ -lattice rapidly transformed into a Δ -crystal. All the Δ/\square interfaces were incoherent, with similar growth speeds; hence, the Δ -lattice nucleus maintained approximately the same shape during growth.

directly into the product phase, the parent phase evolves through intermediate metastable (for example, liquid) states with lower free-energy barriers. However, even in comparison with two-step nucleation during crystallization—for example, ‘liquid \rightarrow dense liquid droplet \rightarrow crystalline nucleus’ (ref. 32) or ‘liquid \rightarrow low-density crystalline nucleus \rightarrow crystalline nucleus’ (ref. 16)—the nature of the s - s nucleation process is remarkable because the intermediate liquid state has a structure that is qualitatively different from both parent and product phases. Regardless, the easy formation of liquid nuclei is plausible from symmetry considerations. In s - s transition theory, each step of the transition is assumed to follow a group-subgroup relation based on symmetry, and a sequence of intermediate states is needed to bridge the parent and product lattices¹³. So far, however, liquid intermediate states have not been considered theoretically¹³. In fact, liquid is an excellent candidate for the intermediate state because the symmetries of all lattices are its subgroups. Consequently, its interfaces might be expected to cost less energy than s - s interfaces. Experimentally, the fluidic intermediate state has been suggested in the graphite–diamond transition on the basis of indirect evidence³³; direct experimental evidence is difficult to come by owing to the very small spatial and rapid temporal scales associated with the intermediate liquid nuclei.

The two-step nucleation occurs only in barrier-crossing processes. When the heating light was switched off, the Δ -lattice nucleus was observed to convert directly back to a \square -lattice without experiencing an intermediate liquid state (Supplementary Movie 6). In this case, the ambient \square -lattice surrounding the nucleus acts effectively as a huge post-critical nucleus, for which a free-energy barrier does not exist.

Nucleation precursor

As well as real-time visualization of the two-step nature of the s - s transition, the novel experimental system enabled exploration of

the early dynamics that lead to nuclei formation. So far, precursors of nucleation have attracted substantial interest in the study of crystal melting^{18,34}, but they have rarely been explored in solid–solid transitions. In our colloidal samples, the nucleation kinetics can be accurately measured because the temperature was fixed during the ~ 10 – 100 min of incubation and nucleation time, which enables easy observation of the liquid nucleation precursors and avoids the catastrophic transitions under strong anisotropic stresses or strong superheating used in many simulations. In the defect-mediated nucleation theory for crystal melting, a perfect crystal develops more and more defects as temperature increases. They diffuse, coalesce and form nuclei above the phase-transition point. Our observations revealed precursors of liquid nuclei in the s - s transition that are not newly generated defects, as is often assumed; rather, they are loop motions similar to those that have been recently observed in crystal melting simulations³⁴ and experiments¹⁸. As shown in Figs 1c, 2a and 3a, particles marked in white leave their lattice sites, but the crystalline structure remains intact; these particles swap positions with neighbours to form closed loops of moving particles in 3D. Indeed, this should be the easiest way to move particles around in a perfect lattice.

In crystals with vacancies, particle swapping can take place in any region, but has a higher chance of occurring near vacancies (Fig. 1c). In crystals with dislocations and/or grain boundaries, particle swapping occurs near dislocations or grain boundaries, and is suppressed in the neighbouring areas (Figs 2a and 3a). Consequently, liquid nucleation starts from dislocations and grain boundaries (Figs 2a and 3a). Vacancies are much more mobile (Fig. 1c,d) than dislocations, and we observed that liquid nuclei formed at vacancies are mobile, whereas liquid nuclei formed around dislocations are pinned; pinning is probably caused by the extra half planes of particles that are associated with dislocations. In the present experiments, attraction or repulsion was not apparent among dislocations (Fig. 2), nor between dislocations and

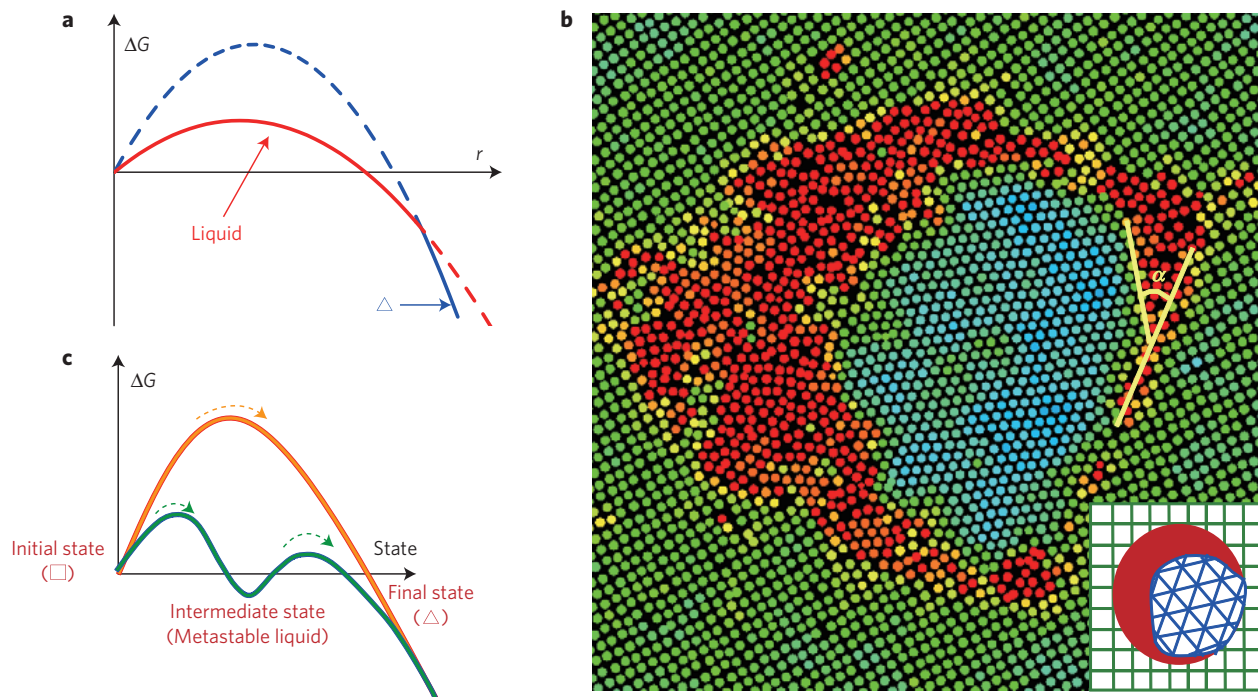


Figure 4 | **Two-step nucleation mechanism.** **a**, Schematic of ΔG for the liquid nucleus (red curve) and the Δ -lattice nucleus (blue curve) forming within the \square -lattice. The combined red-blue solid curve corresponds to the evolution path with the lowest ΔG . $r \propto \sqrt{N}$ is the effective radius of a nucleus with N particles in the xy -plane. The intersection of the red and blue curves corresponds to the liquid- Δ transition process. **b**, The contact angle of the Δ -lattice at the \square - Δ -liquid junction $\alpha < 90^\circ$ (Supplementary Movie 5). The morphology of the nucleus is sketched in the inset, and indicates that the Δ -lattice does not wet the \square -lattice. Colours represent different values of the Lindemann parameter, as shown in Fig. 1. **c**, Ostwald's step rule for the two-step nucleation: the \square -lattice tends to pass through an intermediate metastable liquid state with two lower free-energy barriers, instead of directly transforming into the Δ -lattice. Note that the horizontal axis represents a direction of motion in multidimensional-state space that is different from the horizontal axis in **a**. The crossing point in **a**, however, corresponds to the hopping process over the second barrier in **c**.

liquid nuclei (Figs 2 and 3). Dislocations can diffuse, but they did not drift towards nuclei; rather, they were simply absorbed by an expanding liquid nucleus. Multiple post-critical liquid nuclei were observed to form in crystals with many dislocations. Eventually, they merge and then transform into a Δ -lattice nucleus (Supplementary Movie 5), or transform into Δ -lattice nuclei and then merge.

Growth of nuclei and interface motion

Facets begin to develop after the whole liquid nucleus was transformed into a Δ -lattice. The facets developed earlier in Fig. 2 than in Figs 1 and 3 because the liquid transformed to a triangular lattice faster in Fig. 2, owing to the weaker degree of superheating and the stronger lattice deformation caused by the dislocations (that is, rather than a vacancy or a grain boundary). The facets can be classified into three types according to their structure: a coherent interface with no lattice mismatch (Fig. 2e: I); a semi-coherent interface in which lattice mismatch can be viewed as a chain of dislocations (Fig. 2e: II); and an incoherent interface wherein lattices do not match (Fig. 2e: III–VI). The facets of a nucleus within a crystalline domain cannot be all coherent because a coherent interface requires precise matching between both lattice constants and angles of the two lattices. The slopes in the plots of Fig. 2f give the propagation speeds, v , of various interfaces along the normal (\perp) direction. Notice that the slopes of these lines remain approximately constant during growth, with $v_{\text{coherent}}^\perp < v_{\text{semi-coherent}}^\perp < v_{\text{incoherent}}^\perp$. Moreover, the disordered structure at the incoherent interfaces seems to transform into a thin layer of 'liquid' (red particles in Fig. 2e III–VI), which further enhances the mobility of the particles and the interface³⁵. This behaviour is observed more prominently in the reverse process: after switching

off local heating, the coherent interfaces are pinned, whereas the incoherent interfaces propagate rapidly (Supplementary Movie 6).

The growth of these post-critical Δ -lattice nuclei depends on interface propagation speeds. The propagation speeds of the four incoherent interfaces were similar, which means that the speeds were not very sensitive to the angles between the interface and the two lattices. Furthermore, a fast propagation speed along the normal direction is typically accompanied by a slow propagation speed along the lateral direction; hence, the coherent and semi-coherent interfaces grew faster in the lateral (\parallel) direction—that is, $v_{\text{coherent}}^\parallel > v_{\text{semi-coherent}}^\parallel > v_{\text{incoherent}}^\parallel$. This effect causes the nucleus to elongate, as seen in Fig. 2d,e. Such elongation is energetically favourable because the coherent and semi-coherent interfaces cost less energy than the incoherent interfaces. These interface-propagation behaviours are predicted in theory, and have previously been observed in atomic and molecular polycrystals by electron microscopy¹, although not during the small-scale nucleation process.

Parameters of nuclei

Lastly, the data accumulated from the many experiments permits quantitative determination of a critical-nucleus size, interfacial surface tension, and the distribution of interface angles between the different crystalline solids. The size of the critical liquid nucleus, N^* , is estimated in three ways: from the plateau in the size evolution plots (Fig. 5a), because a critical nucleus is in unstable equilibrium and tends not to grow or shrink; by fitting the $\Delta G(N)$ curve (Fig. 5b) obtained from the Boltzmann distribution of the size of the nuclei³⁶, (Supplementary Information); and from the inflection point of the first-passage time of the nucleus size³⁷ (Supplementary Fig. 4). The three methods yield similar values: $N^* = 50 \pm 20$, 50 ± 10 , 56 ± 20 for the nucleation process shown

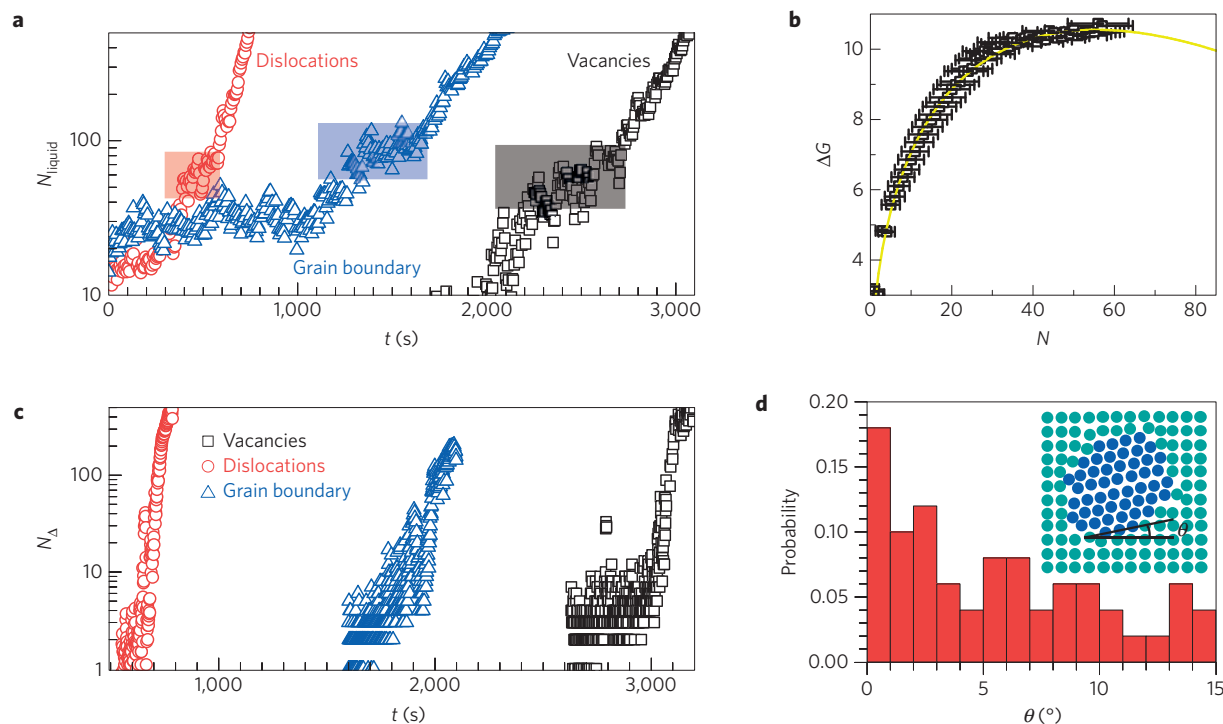


Figure 5 | **Properties of nuclei.** **a**, Size evolution of the liquid nuclei in Figs 1–3. N is the number of particles per layer in the nucleus. The plateaux in the red, blue and black shaded areas correspond to the critical sizes wherein the nuclei were most stable. **b**, The free energy of the liquid nucleus shown in Fig. 1, and fitted by equation (1) (yellow curve). **c**, Size evolution of the Δ -lattice nuclei in Figs 1–3. **d**, Probability distribution of the angle between the \square - and Δ -lattices (inset) in the 50 experiments carried out inside single domains without grain boundaries. Note that the angle ranges from 0 to 15°.

in Fig. 1. For nucleation near dislocations and grain boundaries, the probability of forming a liquid nucleus is not uniform in space. Hence, we estimated the critical size from data in Fig. 5a to be $N^* = 60 \pm 20$ for the case of nucleation near dislocations (Fig. 2) and $N^* = 90 \pm 20$ for the case of nucleation near a grain boundary (Fig. 3). Δ -lattice nuclei grew rapidly in the parent liquid nuclei without a period of steady nuclei distribution; their critical sizes were roughly estimated from Fig. 5c to be $N^* \sim 5$ –30. Fitting of equation (1) to the data in Fig. 5b enabled us to derive an estimate for the surface tension between the liquid nucleus and the superheated square lattice of $\gamma \simeq 0.2 k_B T / \sigma^2$, which is comparable to the value $\gamma \simeq 0.54$ – $0.58 k_B T / \sigma^2$ obtained from simulations of a liquid and a three-dimensional fcc crystal of hard spheres at the melting point³⁸ (Supplementary Information).

Figure 5d shows the broad distribution of the angles between the parent and product lattices found in all 50 experiments carried out inside \square -lattice domains. The angle distribution is consistent with the notion that these transitions are not martensitic, in which case the distribution would have been characterized by a fixed angle between lattices¹. When the Δ -lattice nuclei grew from a liquid/ \square interface, it usually had $0 < \theta < 4^\circ$ (that is, the interfaces were coherent or semi-coherent); those that grew from inside the liquid had $4^\circ < \theta < 15^\circ$ (that is, interfaces were incoherent). For a nucleus with $\theta = 0^\circ$, the Δ - and \square -lattices are aligned such that it can have one or two coherent facets, whereas a nucleus with $\theta \neq 0^\circ$ has no coherent facet. Consequently, a greater number of nuclei with $\theta = 0^\circ$ are seen in Fig. 5d, because coherent interfaces have lower energy.

Outlook

To conclude, we have observed the kinetics of a solid–solid phase transition which very clearly reveals a two-step nucleation process with intermediate liquid state nuclei. The kinetic pathway of a phase transition could involve complicated intermediate states and is often difficult to predict³⁹. Although intermediate

states have been observed in some s–s transitions of molecular crystals¹, all were crystalline intermediate states in martensitic transformations rather than liquid states in diffusive nucleation. Our model for the two-step nucleation mechanism suggests that similar kinetic pathways with an intermediate liquid should generally occur in 2D, 3D and thin-film single crystals and polycrystals when the solid–liquid interfacial energy is lower than the solid–solid interfacial energy. The key controlling factor in the early stages of s–s transformation processes is surface energy, rather than the bulk energies of chemical potential and strain assumed in many s–s transition theories. We note that the interfacial energy in metals and alloys ranges from 500 to 1,000 mJ m^{-2} for incoherent interfaces and from 200 to 500 mJ m^{-2} for semi-coherent interfaces, is less than 200 mJ m^{-2} for coherent interfaces between two crystalline phases, and ranges from 30 to 250 mJ m^{-2} for solid/liquid interfaces¹. Therefore, as the surface of a nucleus cannot be entirely coherent, a liquid nucleus should form in the early stages of s–s nucleation in both single and polycrystalline atomic metals and alloys. The observations show that the barrier for the s–s transition is essentially the barrier for forming a liquid nucleus. Thus, any processing methodology that reduces the energy barrier for liquid nuclei—for example, doping impurities—might lead to a speed-up of sluggish s–s transitions that arise in industrial and metallurgical processes.

In addition, the nucleation precursor of s–s transitions, particle-swapping loops provides a new relaxation mode that makes the s–s transition easier and faster. This new kinetic factor controlling the s–s transition rate should be incorporated in future s–s transition theories.

Our experiments were carried out under isotropic stress, whereas many s–s transitions in nature and in industry are under anisotropic pressure, which enhances the barrier-crossing ability and promotes collective motions of particles. How anisotropic pressure affects

the intermediate liquid and the nucleation precursor is a question worth exploring.

Methods

We synthesized poly(*N*-isopropylacrylamide) (NIPA, pNIPA or pNIPAM) microgel spheres with less than 3% polydispersity and dispersed them in an aqueous buffer solution with 1 mM acetic acid¹⁷. Their pair interactions are measured from the liquid structure of a dilute monolayer of NIPA spheres⁴⁰. The colloidal-sample preparation was the same as that for our thin-film melting experiments in refs 41,42. Briefly, a droplet of the colloidal suspension was placed on a glass slide, then a glass coverslip was placed on the droplet. The glass surfaces were rigorously cleaned to prevent particles sticking to them. The colloidal suspension spread out over most of the 18 × 18 mm² area of the coverslip by capillary force. By adding an appropriate volume of the colloidal suspension before we sealed the sample, we could control the sample cell thickness *H*. For example, a 1.0 μl colloid usually formed four layers at the centre and six layers at the edges in the 18 × 18 mm² sample area. Therefore, there was little wall bending, and the local thickness can be taken as uniform over a ~100 μm field of view. After the droplet spread out over most of the coverslip, the coverslip and the glass slide were glued together with epoxy so that the wall separation *H* was fixed. The cell was filled with colloids and a small amount of air at the edge, so that the viscous epoxy cannot flow into it and affect the wall separation. The epoxy was hardened in air in 5 min. The colloidal spheres formed polycrystals with typical domain sizes ranging from 10 to 100 μm in a freshly made sample. Before the experiment, we used a temperature controller to cycle the temperature to remove small defects and release any pressure that might have built up during spreading out of the droplet before sealing the sample. After annealing near the transition temperature, some domains grew larger than 300 μm in size.

We superheated the interior of the crystal with a beam of light from a 100 W mercury lamp while retaining the ambient temperature below the *s*-*s* transition point (Supplementary Fig. 2A). The area under heating in the focal plane can be set anywhere between 20 μm and 5 mm in diameter by adjusting the iris. We usually set it to 76 μm. We observed the sample in the transmission mode of an upright microscope to avoid direct exposure of the camera to the heating light. A small amount of non-fluorescent black dye (Chromatech-Chromatint black 2232 liquid), 0.6% by volume, was added to the sample to absorb the heating light. The dye seemed to have minor effects on the particle interaction and the phase behaviour. The heating effect can be conveniently measured from $\delta T = T_m - T_m^h$, where T_m^h and T_m are the melting temperatures at a grain boundary with and without the optical heating, respectively. δT depends on the light intensity and the dye concentration, and was usually set to 1.6 °C. A paraffin film was placed in the light path to ensure the optical heating was sufficiently uniform¹⁸. The heating profile shown in Fig. 1a was measured from an aqueous solution of yellow fluorescein (0.01% by weight) in a cell of thickness 5 μm. The brightness of this fluorescent solution is proportional to the light intensity and the heating effect⁴³. The light from the mercury lamp was focused by a ×100 objective, hence the focal plane experienced the strongest heating. In 3D NIPA colloidal crystals¹⁸, the temperature changes by less than 0.2 °C (that is, 0.46% volume fraction) in ±25 layers along the *z* direction, hence the temperature is sufficiently uniform along the *z* direction in a five-layer-thick sample. Indeed, the nucleation behaviours at the top and bottom walls were indistinguishable. Supplementary Fig. 1C shows that the effect of heating stabilized just 3 s after the light was switched on. The lattice constant in the heated region changed by less than 2% and was stabilized in 5 s. Hence sphere diameter and pressure remained constant throughout the entire duration of the incubation and nucleation processes. The temperature gradient in Fig. 1a could induce a small pressure gradient, but it was outside the field of view. Moreover, it reached a steady state 5 s after the light was switched on. Indeed, we observed no flow in the region of interest. Therefore, there was no temperature gradient or pressure gradient in the region of interest. Note that the 0.1 °C resolution of the temperature controller limits slow temperature fluctuations over a timescale of several minutes and that the spatial temperature distribution in the small region of interest is uniform.

Received 2 April 2014; accepted 8 August 2014;
published online 14 September 2014

References

- Porter, D. A., Easterling, K. E. & Sherif, M. Y. *Phase Transformations in Metals and Alloys* (CRC Press, 2008).
- Kirby, S. H., Durham, W. B. & Stern, L. A. Mantle phase changes and deep-earthquake faulting in subducting lithosphere. *Science* **252**, 216–225 (1991).
- Irifune, T., Kurio, A., Sakamoto, S., Inoue, T. & Sumiya, H. Ultrahard polycrystalline diamond from graphite. *Nature* **421**, 599–600 (2003).
- Smith, W. F. *Principles of Materials Science and Engineering* (McGraw-Hill, 1996).
- Erskine, D. J. & Nellis, W. J. Shock-induced martensitic phase transformation of oriented graphite to diamond. *Nature* **349**, 317–319 (1991).
- Khaliullin, R. Z., Eshet, H., Kühne, T. D., Behler, J. & Parrinello, M. Nucleation mechanism for the direct graphite-to-diamond phase transition. *Nature Mater.* **10**, 693–697 (2011).
- Burnley, P. C. & Green, H. W. Stress dependence of the mechanism of the olivine–spinel transformation. *Nature* **338**, 753–756 (1989).
- Jacobs, K., Zaziski, D., Scher, E. C., Herhold, A. B. & Alivisatos, A. P. Activation volumes for solid–solid transformations in nanocrystals. *Science* **293**, 1803–1806 (2001).
- Scandolo, S., Bernasconi, M., Chiarotti, G., Focher, P. & Tosatti, E. Pressure-induced transformation path of graphite to diamond. *Phys. Rev. Lett.* **74**, 4015–4018 (1995).
- Zipoli, F., Bernasconi, M. & Martoňák, R. Constant pressure reactive molecular dynamics simulations of phase transitions under pressure: The graphite to diamond conversion revisited. *Eur. Phys. J. B* **39**, 41–47 (2004).
- Zahn, D. & Leoni, S. Nucleation and growth in pressure-induced phase transitions from molecular dynamics simulations: Mechanism of the reconstructive transformation of NaCl to the CsCl-type structure. *Phys. Rev. Lett.* **92**, 250201 (2004).
- Mundy, C. J. *et al.* Ultrafast transformation of graphite to diamond: An *ab initio* study of graphite under shock compression. *J. Chem. Phys.* **128**, 184701 (2008).
- Toledano, P. & Dmitriev, V. *Reconstructive Phase Transitions in Crystals and Quasicrystals* (World Scientific, 1996).
- Anderson, V. J. & Lekkerkerker, H. N. W. Insights into phase transition kinetics from colloid science. *Nature* **416**, 811–815 (2002).
- Gasser, U., Weeks, E. R., Schofield, A., Pusey, P. N. & Weitz, D. A. Real-space imaging of nucleation and growth in colloidal crystallization. *Science* **292**, 258–262 (2001).
- Tan, P., Xu, N. & Xu, L. Visualizing kinetic pathways of homogeneous nucleation in colloidal crystallization. *Nature Phys.* **10**, 73–79 (2014).
- Alsayed, A. M., Islam, M. F., Zhang, J., Collings, P. J. & Yodh, A. G. Premelting at defects within bulk colloidal crystals. *Science* **309**, 1207–1210 (2005).
- Wang, Z., Wang, F., Peng, Y., Zheng, Z. & Han, Y. Imaging the homogeneous nucleation during the melting of superheated colloidal crystals. *Science* **338**, 87–90 (2012).
- Savage, J. R., Blair, D. W., Levine, A. J., Guyer, R. A. & Dinsmore, A. D. Imaging the sublimation dynamics of colloidal crystallites. *Science* **314**, 795–798 (2006).
- Weeks, E. R., Crocker, J. C., Levitt, A. C., Schofield, A. & Weitz, D. A. Three-dimensional direct imaging of structural relaxation near the colloidal glass transition. *Science* **287**, 627–631 (2000).
- Zhang, Z. *et al.* Thermal vestige of the zero-temperature jamming transition. *Nature* **459**, 230–233 (2009).
- Yethiraj, A., Wouterse, A., Groh, B. & van Blaaderen, A. Nature of an electric-field-induced colloidal martensitic transition. *Phys. Rev. Lett.* **92**, 058301 (2004).
- Weiss, J. A., Oxtoby, D. W., Grier, D. G. & Murray, C. A. Martensitic transition in a confined colloidal suspension. *J. Chem. Phys.* **103**, 1180–1190 (1995).
- Bolhuis, P. & Frenkel, D. Prediction of an expanded-to-condensed transition in colloidal crystals. *Phys. Rev. Lett.* **72**, 2211–2214 (1994).
- Casey, M. T. *et al.* Driving diffusionless transformations in colloidal crystals using DNA handshaking. *Nature Commun.* **3**, 1209 (2012).
- Pieranski, P., Strzelecki, L. & Pansu, B. Thin colloidal crystals. *Phys. Rev. Lett.* **50**, 900–903 (1983).
- Schmidt, M. & Löwen, H. Freezing between two and three dimensions. *Phys. Rev. Lett.* **76**, 4552–4555 (1996).
- Fortini, A. & Dijkstra, M. Phase behaviour of hard spheres confined between parallel hard plates. *J. Phys. Condens. Matter* **18**, L371–L378 (2006).
- Mitchell, T. B. *et al.* Direct observations of structural phase transitions in planar crystallized ion plasmas. *Science* **282**, 1290–1293 (1998).
- Narasimhan, S. & Ho, T.-L. Wigner-crystal phases in bilayer quantum Hall systems. *Phys. Rev. B* **52**, 12291–12306 (1995).
- Crocker, J. C. & Grier, D. G. Methods of digital video microscopy for colloidal studies. *J. Colloid Interf. Sci.* **179**, 298–310 (1996).
- Ten Wolde, P. R. & Frenkel, D. Enhancement of protein crystal nucleation by critical density fluctuations. *Science* **277**, 1975–1978 (1997).
- Shekar, N. C. & Rajan, K. G. Kinetics of pressure induced structural phase transitions. *Bull. Mater. Sci.* **24**, 1–21 (2001).
- Bai, X.-M. & Li, M. Ring-diffusion mediated homogeneous melting in the superheating regime. *Phys. Rev. B* **77**, 134109 (2008).
- Levitas, V. I., Henson, B. F., Smilowitz, L. B. & Asay, B. W. Solid–solid phase transformation via virtual melting significantly below the melting temperature. *Phys. Rev. Lett.* **92**, 235702 (2004).

36. Auer, S. & Frenkel, D. Prediction of absolute crystal-nucleation rate in hard-sphere colloids. *Nature* **409**, 1020–1023 (2001).
37. Lundrigan, S. E. & Saika-Voivod, I. Test of classical nucleation theory and mean first-passage time formalism on crystallization in the Lennard-Jones liquid. *J. Chem. Phys.* **131**, 104503 (2009).
38. Davidchack, R. L. Hard spheres revisited: Accurate calculation of the solid–liquid interfacial free energy. *J. Chem. Phys.* **133**, 234701 (2010).
39. Evans, R. M. L., Poon, W. C. K. & Renth, F. Classification of ordering kinetics in three-phase systems. *Phys. Rev. E* **64**, 031403 (2001).
40. Polin, M., Grier, D. G. & Han, Y. Colloidal electrostatic interactions near a conducting surface. *Phys. Rev. E* **76**, 041406 (2007).
41. Peng, Y., Wang, Z., Alsayed, A. M., Yodh, A. G. & Han, Y. Melting of colloidal crystal films. *Phys. Rev. Lett.* **104**, 205703 (2010).
42. Peng, Y., Wang, Z., Alsayed, A. M., Yodh, A. G. & Han, Y. Melting of multilayer colloidal crystals confined between two walls. *Phys. Rev. E* **83**, 011404 (2011).
43. Jiang, H., Wada, H., Yoshinaga, N. & Sano, M. Manipulation of colloids by a nonequilibrium depletion force in a temperature gradient. *Phys. Rev. Lett.* **102**, 208301 (2009).

Acknowledgements

This work was supported by Chinese grants NSFC11374248 (Y.H.), NSFC11004143, NSFC21174101, NSFC91027040 and NBRPC.2012CB821500 (Z.Z.), and by US grants NSF DMR12-05463, NSF-MRSEC DMR11-20901 and NASA NNX08AO0G (A.G.Y.).

Author contributions

Y.P. and Y.H. conceived and designed the research plan. Y.P. carried out the experiment and data analysis with help from Z.W. F.W., Y.P. and Y.H. carried out the theoretical modelling. A.M.A. and Z.Z. synthesized the particles. Y.H., Y.P. and A.G.Y. wrote the paper. Y.H. and A.G.Y. supervised and supported the work. All authors discussed the results.

Additional information

Supplementary information is available in the online version of the paper. Reprints and permissions information is available online at www.nature.com/reprints. Correspondence and requests for materials should be addressed to Y.H.

Competing financial interests

The authors declare no competing financial interests.